On the Nature of the Teleseismic Pn Phase Observed on the Ultralong-Range Profile "Quartz," Russia

Article *in* Bulletin of the Seismological Society of America · February 1998

CITATIONS
43

READS
46

4 authors, including:

Scott B. Smithson
University of Wyoming
177 PUBLICATIONS **3,982** CITATIONS

SEE PROFILE

Bulletin of the Seismological Society of America, Vol. 88, No. 1, pp. 62–73, February 1998

On the Nature of the Teleseismic P_n Phase Observed on the Ultralong-Range Profile "Quartz," Russia

by Igor B. Morozov, Elena A. Morozova, Scott B. Smithson, and Leonid N. Solodilov

Abstract The most prominent secondary phase observed in the records from the ultralong profile "Quartz" crossing northern Eurasia is the high-frequency long-range (teleseismic) P_n. This phase, propagating with the group velocity of about 8.1 to 8.2 km/sec to over 3000 km distances, dominates the records within the frequency range above about 5 Hz. Within this teleseismic P_n, we distinguish onsets of several branches having higher apparent velocities between 8.5 and 8.6 km/sec. Using travel-time modeling techniques, we associate the teleseismic P_n with whispering gallery modes traveling within the top 160 km of the mantle. The long incoherent coda of this phase results from scattering and from reverberations of seismic waves within the crust. The contrast in frequency contents between the teleseismic P_n and deeper refracted and reflected phases is explained by the increase of inelastic attenuation within the prominent low-velocity zone (LVZ) below the depth of about 150 km.

Introduction

The Russian Deep Seismic Sounding (DSS) program produced unparalleled, until now, seismic datasets suitable for a detailed study of the seismic structure of the upper mantle. A characteristic feature of this program was the use of large chemical and nuclear explosions (powerful nuclear explosions, PNEs) recorded by densely spaced (10 to 15 km), three-component, short-period (1 to 2 Hz) portable recording systems deployed along linear profiles. Recording ranges of PNEs exceeded 3000 km, allowing observations of seismic phases diving down to 800 km into the mantle (Egorkin and Pavlenkova, 1981; Ryaboy, 1989; Kozlovsky, 1990). The data from one of the best profiles of this program, "Quartz" acquired during 1984 through 1987, have been extensively studied by several groups, providing information about the mantle structure (Mechie *et al.*, 1993; Ryberg *et al.*, 1995, 1996) and about the structure of the crust (Egorkin and Mikhaltsev, 1990; Schueller *et al.*, 1997) of the northern Eurasia (Fig. 1).

PNE records from Quartz profile show a consistent sequence of primary *P*-wave refractions in the first arrivals observed to the maximum offset of 3145 km (Fig. 2). Based on the analysis of the first arrivals, Mechie *et al.* (1993) derived 1D velocity models for different PNEs, and Ryberg *et al.* (1996) proposed a 2D model of the mantle velocity structure, using all three PNEs of the profile (Fig. 1).

Due to high energy of the sources, PNE records are abundant in seismic phases as secondary arrivals (Fig. 2). Reflections from the 410- and 660-km discontinuities in the mantle and a number of crustal multiples are easily recognized (Fig. 2). Reversed PNE records reveal horizontal variations in the structure of the mantle within the length of the profile (Ryberg *et al.*, 1996; Morozova *et al.*, 1997). This article concentrates on the phase that is not obvious in unfiltered gathers but becomes dominant after high-pass filtering of the records above approximately 5 Hz (Figs. 3 and 4). This phase is also observed in the radial and transverse components and in the records from the third PNE of Quartz profile (see plots in Ryberg *et al.*, 1995).

Such high-frequency, long-range (often called teleseismic) P_n phases, and corresponding S_n phases propagating within the uppermost mantle to 2000- to 3000-km distances were observed by many authors (e.g., Molnar and Oliver, 1969; Heustis *et al.*, 1973; Walker 1977). These phases efficiently propagate through continental shields and deep-ocean basins but appear to be blocked by major suture zones (Molnar and Oliver, 1969). Although it is generally accepted that these phases are due to some sort of wave-guide mechanism, no agreement about the details of this mechanism exists. Depending on the mantle structure beneath the Moho, several models of these high-frequency, long-range phases have been proposed: whispering-gallery (WG) waves within the upper mantle (Stephens and Isacks, 1977; Menke and Richards, 1980), guided wave in a high-velocity layer above a low-velocity layer (Mantovani *et al.*, 1977), or transmission through a low-velocity layer beneath the Moho (Sutton and Walker, 1972). Long incoherent codas of teleseismic P_n and S_n arrivals are explained by scattering of high-frequency waves within the crust and upper mantle (Richards and Menke, 1983; Menke and Chen, 1984) together with reverberations in the water column (Sereno and Orcutt, 1985, 1987).

Ryberg *et al.* (1995), who first observed this band of

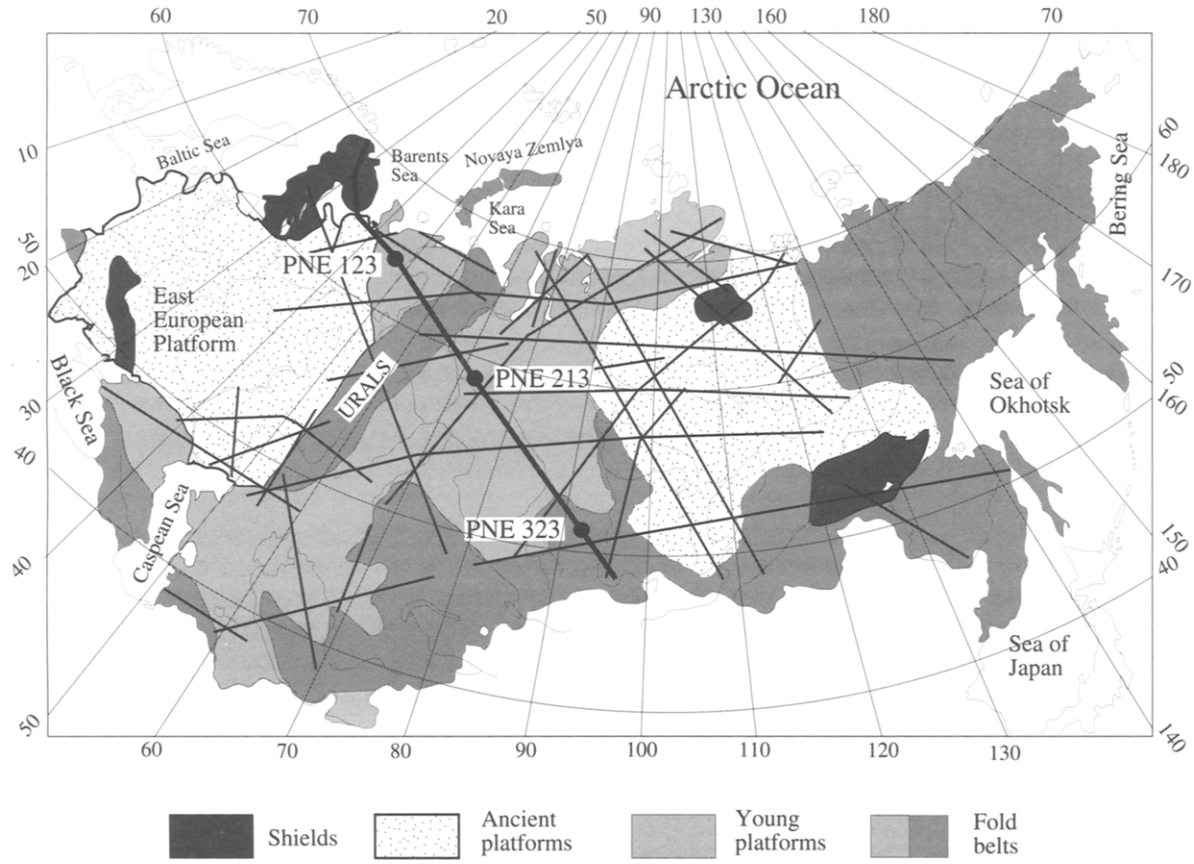

Figure 1. Map of the former USSR showing major DSS profiles using nuclear explosions. Quartz is shown in bold line; circles indicate the locations of three nuclear explosions recorded by the profile. The data from the southern and northern PNEs (shot points 323 and 123) are used in this article.

incoherent high-frequency energy in Quartz records, proposed a model that relates this phase to a special propagation mechanism through a strongly scattering wave guide located immediately below the Moho. Using simulations with the *reflectivity* method (Fuchs and Müller, 1971), Tittgemeyer *et al.* (1996) demonstrated that a high-frequency phase with an apparent velocity of about 8.1 km/sec can propagate by means of multiple scattering through an 80-km-thick stochastic sequence of thin layers below the Moho.

Although presenting a possible propagation mechanism, this "multiply scattering wave guide" by Ryberg *et al.* (1995) and Tittgemeyer *et al.* (1996) does not appear to be the likely solution, since it implies very strong horizontal continuity of the scatterers. Strongly scattering mantle above 120 km would have been clearly recognized in earthquake codas. From the observational standpoint, this model does not account for three important details of the kinematics of this high-frequency phase in Quartz records: (1) the increase in its apparent velocity within the offset range of 1000 to 1700 km; (2) the separation of its onset into at least three branches with apparent velocities of about 8.5 to 8.6 km/sec between the offsets of 1300 and 2400 km; and (3) the presence of a high-frequency and high-velocity event at the offsets exceeding 2700 km, and 7 to 10 sec before the main teleseismic P_n (Fig. 4). Also, the scattering–wave-guide model does not explain the relation of the teleseismic P_n to other low-frequency phases and, in particular, the coincidence of the onset of this phase with the "internal multiple" *m* indicated earlier by Mechie *et al.* (1993) within the offset range 1000 to 1700 km (Fig. 2). Finally, the unfiltered records from PNE 123 show that the teleseismic P_n between the offsets of 900 and 1700 km is remarkably strong and coherent (Fig. 3), and therefore, it definitely cannot be due to a stochastic scattering mechanism.

As it often happens in seismology, another interpretation of these observations exists. In this article, we re-examine the nature of the teleseismic P_n in Quartz records. After analyzing travel-time, amplitude, and spectral characteristics of a number of secondary phases, and after performing a simple simulation of scattering within the crust, we arrived at a model of teleseismic P_n propagation that is different from the stochastic model by Ryberg *et al.* (1995) and Tittgemeyer *et al.* (1996), but it is related to the more deterministic WG models proposed earlier (Menke and Rich-

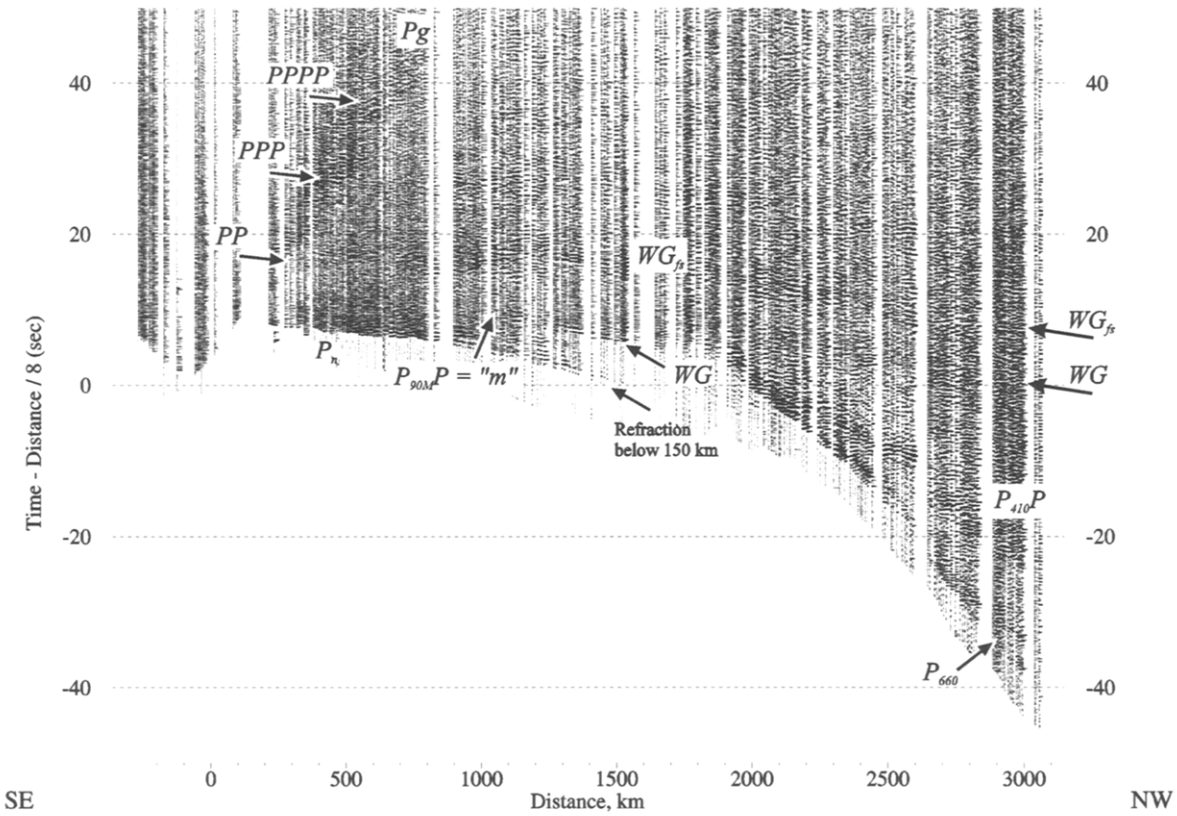

Figure 2. Vertical-component record section from the southern PNE 323 of profile Quartz. This PNE is characterized by the highest amplitude of high-frequency signal. Reduction velocity is 8 km/sec. Primary refractions (P_n, P_{410}, P_{660}), P_g, reflection from the 410-km discontinuity ($P_{410}P$), Moho multiple from 90 km depth ($P_{90M}P$, labeled as "*m*" by Mechie *et al.*, 1993), and the first whispering-gallery (WG) mode discussed in this article are indicated. The WG mode is followed by a multiple, which we associate with the free-surface WG mode (WG_{fs}). At offsets below 1500 km, a series of Moho multiples can be seen (*PP, PPP, PPPP*).

ards, 1980). Figure 5 summarizes the main idea of our interpretation. Instead of speaking of the "high-frequency" teleseismic P_n, we recognize it as the first "broadband" arrival at offsets exceeding 1000 km, in comparison to which the deeper refracted and reflected waves are relatively devoid of high-frequency energy. This observed penetration, depth-dependent frequency selectivity is associated with the increase of seismic attenuation with depth.

Teleseismic P_n in Quartz Records

Analyzing the nature of the incoherent high-frequency teleseismic P_n phase in Quartz records, we explain three major observed characteristics of this phase:

1. its travel-time dependence and relations to other seismic phases;
2. clear separation in frequency content from the lower-frequency deep refractions; and
3. its incoherence and the long incoherent coda.

Starting our analysis with the first characteristic, and after travel-time forward modeling of the major phases contributing to the observed wave field, we present a simple simulation of the kinematic effects of scattering in the first-order Born approximation. After this, we describe how the attenuation within the upper mantle can cause the observed frequency separation of the teleseismic P_n from deep mantle refractions. After that, we briefly discuss the possible role of scattering effects in the formation of the coda.

In the subsequent analysis, we use the records of the southern Quartz PNE (shot point 323 in Fig. 1) having the largest signal-to-noise ratio within the high-frequency part of recorded bandwidth (Fig. 2).

Phase Correlation

The critical difference of our interpretation from that by Ryberg *et al.* (1995) lies in a different identification of the seismic phases (Fig. 6). In the high-frequency filtered gathers (Fig. 4), we see that the teleseismic P_n increases its apparent velocity toward smaller offsets, between 1000 and 1500 km, where it is close to the Moho multiple from the depth of about 90 km (Fig. 6). The continuation of this phase

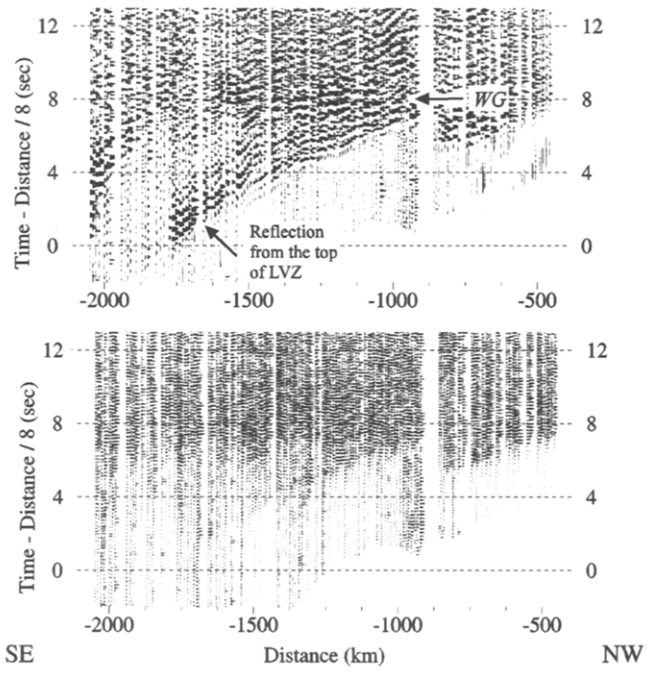

Figure 3. A segment of the vertical-component record section from the northern PNE 123 between the offsets 500 and 2000 km SE of the source point (Fig. 3). (*Top*) unfiltered records; (*bottom*) the same records after high-pass filtering above 5 Hz. Reduction velocity is 8 km/sec. Note the strong and coherent whispering-gallery phase (*WG*) propagating above the level of approximately 150 km and dominating the high-frequency records. This phase is also strong and coherent in the unfiltered records between the offsets of 900 and 1600 km. Also note the strong reflection from the top of the asthenospheric LVZ beginning at about 200 km depth. This reflection is practically absent from the high-frequency gather, indicating the increase of attenuation between the depths of 150 and 200 km.

toward the ordinary P_n is clearly of a significantly lower amplitude, and it is not seen in Figure 4. Teleseismic P_n becomes visible in the records (Fig. 4) only near the triplication point of the first WG wave, following the onset of the Moho multiple from the depth of 90 km (Fig. 6). This observation also argues against the "scattering wave guide" origin of the teleseismic P_n, since such scattering would have resulted in a uniformly decreasing amplitude with offset. Between the offsets of 1500 and 2700 km, the onset of the teleseismic P_n is apparently discontinuous, with a cusp near 2300 km (Fig. 4). This travel-time pattern most likely corresponds to two WG branches with apparent velocities near 8.6 km/sec (Fig. 6).

Travel-Time Analysis

To examine the travel-time pattern of seismic phases found in the records, we employ 2D raytracing in a spherically symmetric 1D model. Although raytracing does not account for wave interference effects and cannot correctly predict amplitude variations in the presence of sharp velocity contrasts and shadow zones, it is still an excellent tool providing an insight into mutual relations between different types of seismic waves. Using raytracing, hypotheses about the origins of certain phases can be formulated and easily tested for correct kinematics. Shooting at controlled angular intervals, we in many cases can approximately estimate relative amplitudes of the waves by comparing ray densities at receiver points or by calculating wave-front curvatures (Cerveny *et al.*, 1984).

To explain the principal relations of the observed seismic phases, the 1D model developed using the first breaks picked from the records of the same southern PNE is quite appropriate (Mechie *et al.*, 1993; Fig. 7). The velocity column associated with this PNE is characterized by a strong velocity gradient between 90 and 120 km, a narrow low-velocity zone (LVZ) between 140 and 155 km, and a prominent LVZ with a moderate velocity gradient between 195 and 380 km depth. The 410-km discontinuity is placed at 420 km in this model. This velocity structure explains the first breaks very well, including the 400-km-long shadow zone between the offsets from 1500 to 1900 km (Fig. 2; see also Mechie *et al.*, 1993). The quality of the first arrivals from all three Quartz PNEs, and especially from the southern PNE, is high and allows a confident identification of described velocity gradients within the upper mantle. Although certain difficulties are encountered in the integration of this velocity column with that corresponding to the northern PNE (Mechie *et al.*, 1993; Ryberg *et al.*, 1996), these difficulties do not affect our interpretation of the upper-mantle-guided seismic phases.

The results of our travel-time modeling of the main phases propagating in this 1D velocity structure are summarized in Figure 8 and are compared to the high-frequency record section in Figure 9. As Figure 9 shows, the first WG mode corresponds to the observed teleseismic P_n throughout its entire observation length. The WG mode appears at offsets of about 400 to 500 km and has a significant amplitude in between the offsets of 1500 and 2000 km, representing the first strong arrival in this region. Toward smaller offsets, its travel-time curve can be continued as that of a multiple between a reflector at about 90 km depth and the Moho, as labeled in Figure 2. At larger offsets, this phase continues to the end of the offset range with an apparent group velocity of 8.2 km/sec. (Fig. 8). Note that the second WG mode appearing at the offsets of about 2200 km can be also identified in the records (compare Fig. 4 with Fig. 9). Due to the variations of the velocity gradient above 140 km depth (Fig. 7), this WG mode exhibits a triplication near 1800 to 2000 km, with the fast branch having an apparent velocity of 8.7 to 8.8 km/sec (Fig. 8). Both WG branches are barely visible in unfiltered records (Fig. 2) but become discernible in the high-pass filtered records of Figure 9, after the low-frequency reverberations of the first arrivals have been attenuated.

Based on the foregoing observations—on the high am-

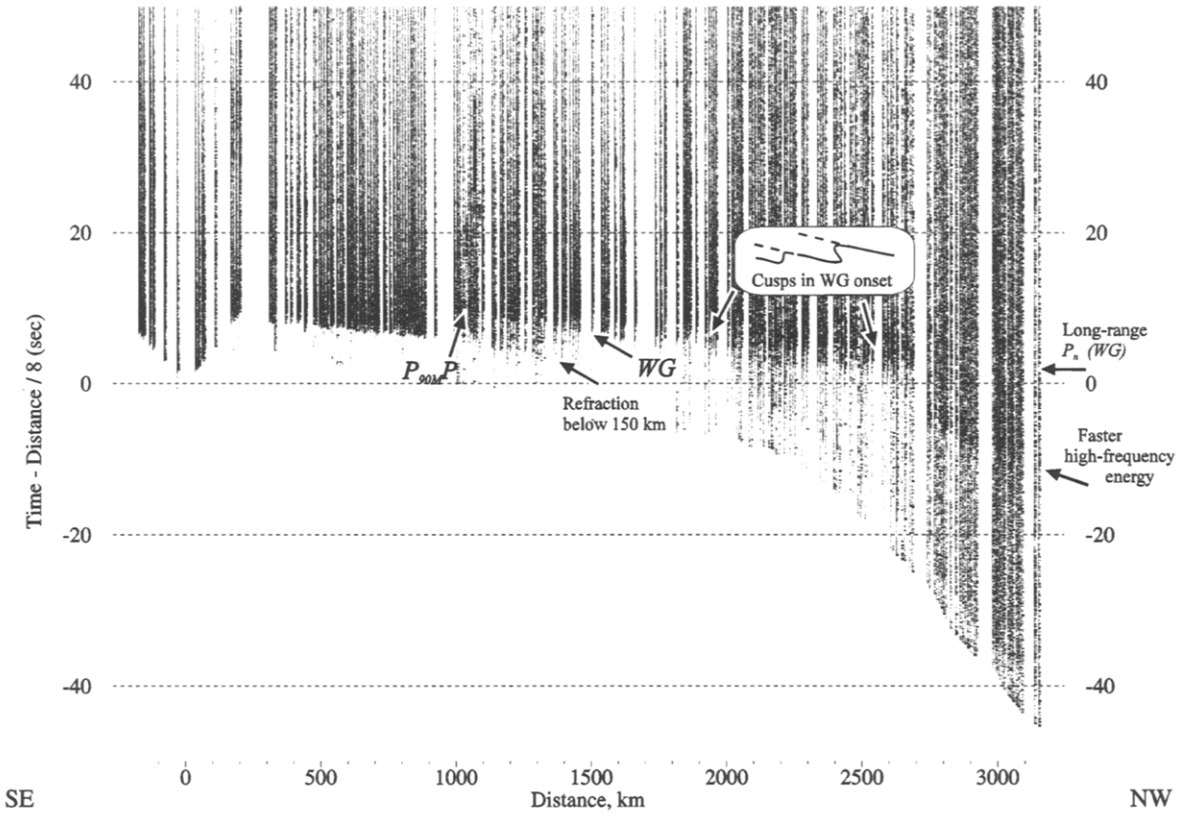

Figure 4. Three-component instantaneous vector amplitude gather of high-pass filtered records from the southern PNE, obtained using the technique described by Morozov and Smithson (1996). Vector amplitude provides a more stable amplitude pattern facilitating the identification of the WG modes. Reduction velocity is 8 km/sec, corner frequency of the filter 5 Hz. This record is dominated by a band of energy propagating with an apparent velocity of about 8.1 km/sec, corresponding to the teleseismic P_n phase. Despite an incoherent nature of its onset, two branches (before and after 2300 km) can be distinguished. We associate this phase with two low-order whispering-gallery (*WG*) modes. Note high-frequency energy with faster apparent velocity arriving 7 to 10 sec earlier than this band at distances exceeding 2700 km.

plitude of the WG phase observed from 1500 to 2000 km of offset in unfiltered records, on the travel-time match of this phase with the teleseismic P_n throughout the entire offset range, and on the observation of the triplication of the teleseismic P_n at about 2000 km—we conclude that the WG mode presents a good explanation of the kinematics of the observed teleseismic P_n phase. As we see in Figures 3 and 4, the travel-time curve of the long-range P_n *does not* approach that of the ordinary P_n with decreasing offsets but follows the moveout of a multiple reflection from a depth of approximately 90 km. Therefore, the long-range P_n cannot originate immediately below the Moho, as was suggested by Ryberg *et al.* (1995) and Tittgemeyer *et al.* (1996), but should effectively be produced by the velocity gradient between 90 and 120 km depth (Fig. 7).

A significant feature of the high-frequency wave field is the presence of energy propagating earlier and faster than the teleseismic P_n at offsets exceeding 2700 km (Fig. 4; it is also labeled in Fig. 9. Note, however, that recording systems of a different type were used at the offsets above 2700 km, and thus the records may look more discontinuous across the White Sea). The calculated fast travel-time branch WG_1 has a correct travel-time placement and moveout but terminates at offsets of about 2700 km due to its plunging into the LVZ (Fig. 8). This inconsistency of the model is apparently due to its simplified 1D character and should be resolved in a future 2D model that will include the information from refracted, reflected, and WG waves from all three PNEs. Most likely, the increased amplitude of the WG_1 mode at far offsets marks the termination and/or deepening of the asthenospheric LVZ toward the Baltic Shield.

High Frequency of the Long-Range P_n: A Constraint on the Attenuation within the Upper Mantle

A simple "first-order" explanation of the differences in frequency contents of the seismic phases shown in Figures 2 and 4 is readily obtained from an examination of the penetration depth diagram shown in Figure 8. The near-offset

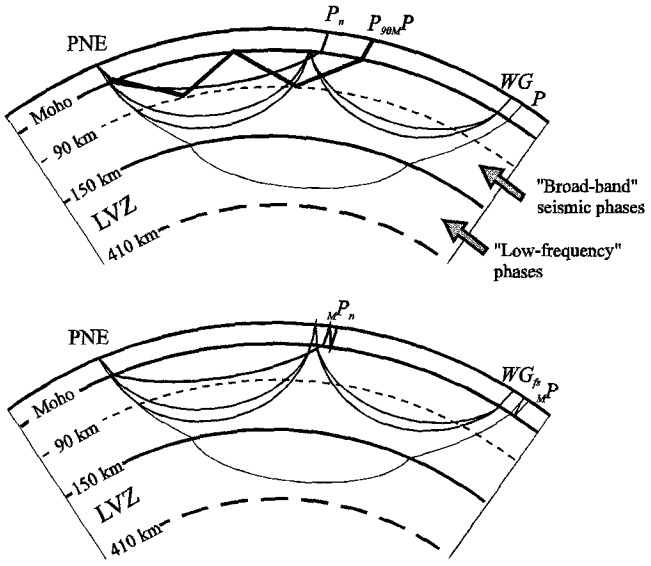

Figure 5. A summary of our interpretation of observed high-frequency phases in Quartz records. Not drawn to scale. (*Top*) P_n, refracted waves turning above the low-velocity zone (LVZ); $P_{90M}P$, multiple reflection from the 90-km boundary and from the Moho; *WG*, whispering-gallery modes (multiple refractions); *P*, far-offset deep refraction arriving depleted of high-frequency energy. Triplication of WG modes due to the velocity contrast within the 80- to 120-km-depth range is indicated by double ray paths. As shown, all broadband phases (P_n, $P_{90M}P$, and *WG*) do not penetrate into the LVZ, whereas the "low-frequency" phases arriving beyond the offset of 1000-km travel within the LVZ for over 150 sec. (*Bottom*) Examples of major Moho multiples contributing to the coda pattern: ${}_MP_n$, P_n multiple; ${}_MP$, multiple of the teleseismic turning wave; WG_{fs}, free-surface WG mode. Other first-order multiples of these phases (not shown for clearness) can be constructed by including a ray bouncing within the crust into other branches of the corresponding rays.

high-frequency refracted mantle wave seen up to nearly 1500 km offset is significantly attenuated beyond the distance of 1000 km (Figs. 2 and 4), which corresponds to the penetration depth of about 150 km (Fig. 8). Likewise, the high-frequency WG modes observed between the offsets of 800 and 2800 km do not dive deeper than about 150 km into the mantle. On the contrary, the deeper and faster branch WG_1 is significantly attenuated between 2000 and 2700 km of offset (Fig. 9). In addition, Figure 8 shows that all far-offset and low-frequency refractions penetrate at least to the depth of 270 km. All these observations suggest that the low-velocity structures below the level of 150 km may cause attenuation sufficient to explain the observed amplitude decay of the deeper phases at the frequencies near and above 5 Hz. Since the total propagation times of the deep phases are *smaller* than those of the wave-guide modes, a significant increase in the attenuation should occur below the depth of about 150 km.

Although the depth level at which the increase of the attenuation occurs is constrained by the above observations as close to 150 km, its accuracy is limited by the use of the 1D velocity model (Fig. 7) and by the ray-theoretical approximation employed. Therefore, we do not attempt to obtain a more precise estimate for the depth of the contrast, or to correlate our 1D attenuation model with the detailed velocity column shown in Figure 7. Instead, we assume a simple two-layer attenuation structure, with the quality factors Q above the level of 150 km and Q_{LVZ} below it, and look for a relation $Q_{\mathrm{LVZ}}(Q)$ between them.

To constrain the amount of the attenuation increase, we calculate the relative energy dissipation factor between two selected frequencies during the propagation of a deep refracted wave:

$$A_{12}^{\mathrm{deep}} = 10 \cdot \lg\left(\frac{E(f_1)}{E(f_2)}\right) = 10 \cdot \lg e \cdot \left(\frac{2\pi}{Q} t_s + \frac{2\pi}{Q_{\mathrm{LVZ}}} t_d\right)(f_2 - f_1). \quad (1)$$

This equation describes the increase in the ratio of the low-frequency spectral density (frequency f_1) to the high-frequency spectral density (frequency f_2), in dB. In this equation, the times that the deep refracted wave travels above and below the depth of 150 km are denoted as t_s and t_d, respectively. Subtracting from the quantity defined in equation (1) a similar ratio for WG arrival, we obtain an expression for the observed logarithmic relative contrast between the two spectral constituents of these phases:

$$A_{12}^{\mathrm{deep}} - A_{12}^{\mathrm{waveguide}} = 10 \cdot \lg e \cdot \left(\frac{2\pi}{Q} t_s + \frac{2\pi}{Q_{\mathrm{LVZ}}} t_d - \frac{2\pi}{Q} t_{wg}\right)(f_2 - f_1), \quad (2)$$

where t_{wg} is the total travel time of the WG mode, taken at the same offset.

Note that the relative spectral densities calculated for the same type of phase in equation (1) are independent of the receiver coupling variations, of the geometrical spreading factors, and of the Moho reflection coefficients (for WG phase) but depend on the source amplitude spectrum. The second relative spectral ratio given in equation (2) does not depend on the source spectrum, and therefore, it is suitable for attenuation estimates.

The relative spectral ratios (2) for two frequency bands 1.0 to 1.5 Hz and 4 to 6 Hz measured in the records between the offsets of 2000 and 2500 km are presented in Figure 10. As Figure 10 shows, the power spectral density in the first arrivals is by 10 to 12 dB lower than that in the teleseismic P_n. By using this value as the estimate of the spectral contrast, by picking characteristic travel times for these offsets from the plots in Figure 8 ($t_a \approx 200$ sec, $t_s + t_d \approx 250$ sec,

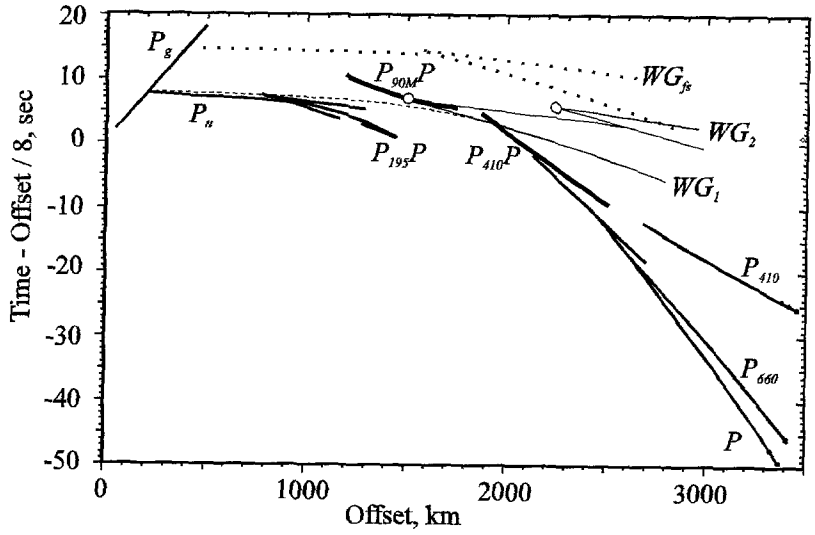

Figure 6. A sketch of the travel-time curves of the seismic phases identified in Figures 2 and 4. Solid lines represent primary refractions and WG modes. Dashed line shows the low-amplitude near-offset part of the WG travel-time curve. Note the onsets of different whispering-gallery modes WG_1 and WG_2 that we associate with the observed undulations of the teleseismic P_n onset between 1500 and 2700 km (Fig. 4). Thick lines represent the reflections from the top of the main LVZ ($P_{195}P$), from the 410-km discontinuity ($P_{410}P$), and Moho multiple from the depth of 90 km ($P_{90M}P$). Free-surface WG mode (dotted line, WG_{fs}) contributes to the coda of the teleseismic P_n. Solid gray circles indicate triplication points of the primary WG modes. See discussion in the text.

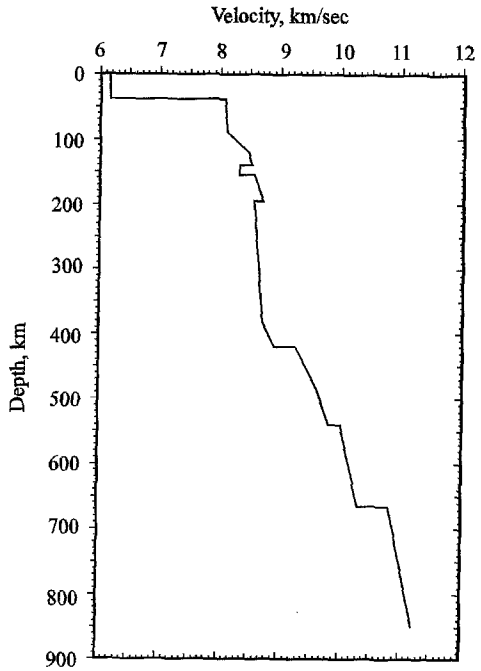

Figure 7. One-dimension velocity model obtained by Mechie *et al.* (1993) using first arrivals from the southern PNE. We used this model for 2D raytracing in our analysis of the kinematics of the teleseismic P_n. Note a LVZ between 140 and 155 km depth and a prominent LVZ below 195 km.

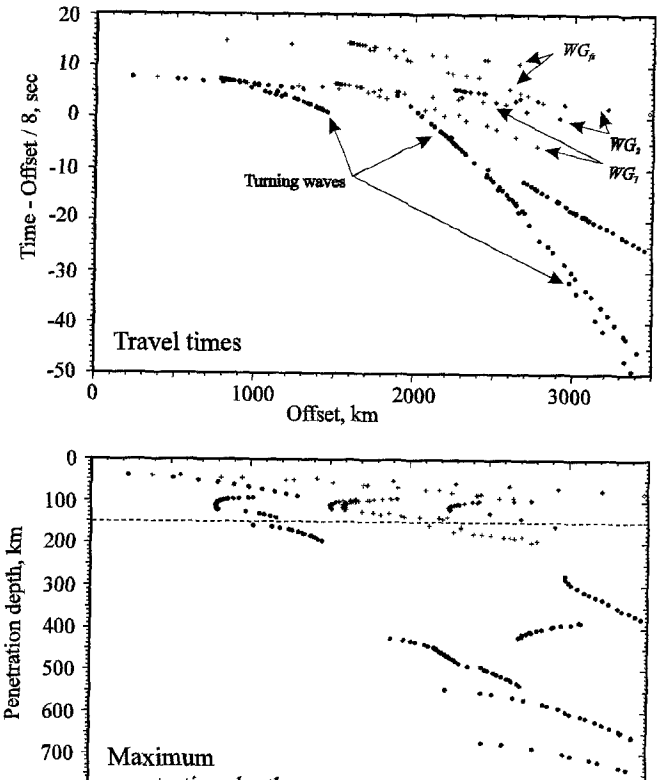

Figure 8. (*Top*) Travel-time curves of the major phases. (*Bottom*) Maximum penetration depths of refracted waves. Note that all "low-frequency" waves arriving before WG modes penetrate into the two LVZs (Fig. 7).

and $t_g \approx 260$ sec), and by varying Q, we obtain from equation (2) the relation for the quality factor $Q_{LVZ}(Q)$ below the 150-km level shown in Figure 11. Although this estimate does not constrain the attenuation in the uppermost mantle, it demonstrates that a significant increase in attenuation below the 150-km level is necessary to explain the observed difference in the high-frequency content between the more shallow and deep refractions and reflections (Fig. 11). Assuming that the attenuation above the LVZ corresponds to $Q \approx 400$ to 600 (Anderson and Given, 1982), we obtain from equation (2) values $Q_{LVZ} \approx 320$ to 400 for the quality factor below the 150-km level (Fig. 11). Note that the contrast between the attenuation above and within the LVZ increases with increasing Q.

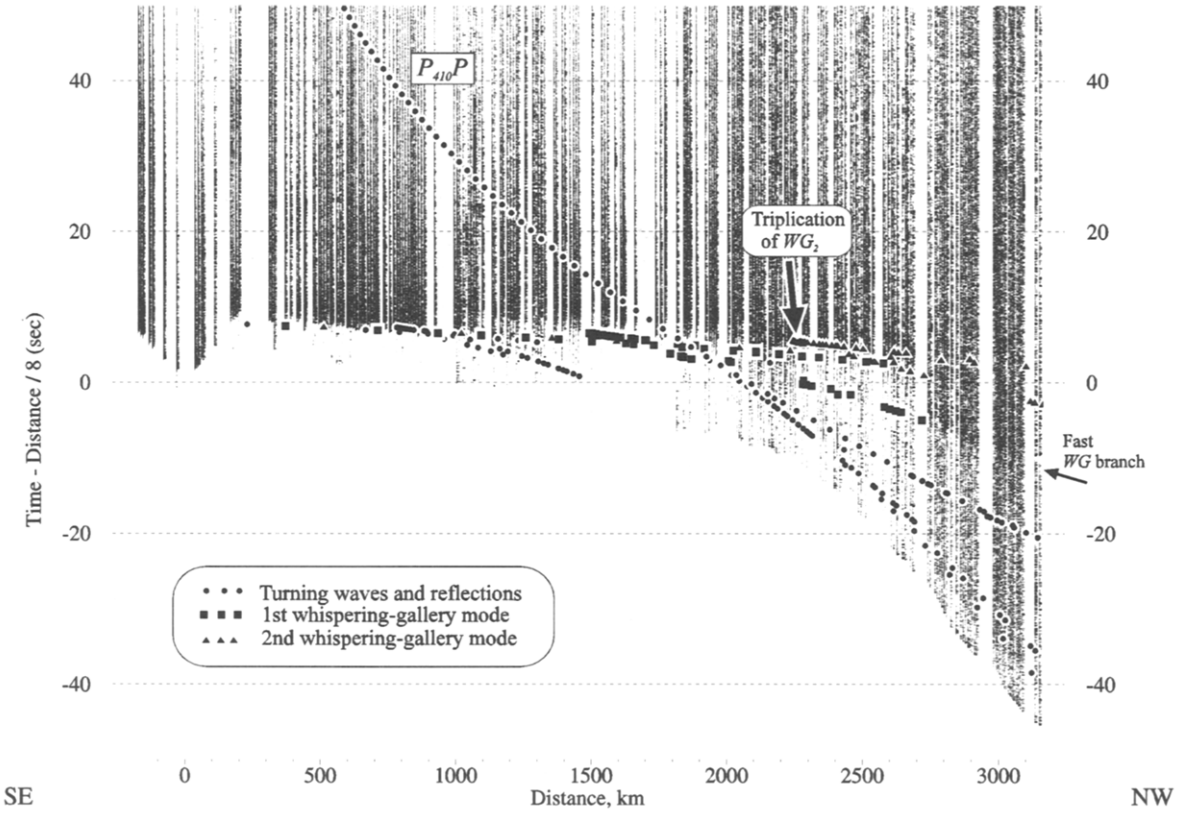

Figure 9. The same travel-time points as in Figure 8 overlain over the high-pass filtered record shown in Figure 4. WG modes correspond to the onset of the high-frequency teleseismic P_n. Note the triplication point of the second WG mode, also seen as a cusp in the onset of the teleseismic P_n in Figure 4. The fast branch of WG mode is observed but can be followed to farther distances than in the modeled travel-time curves (indicated by an arrow on the right side of the section). Travel-time curve of the reflection from the 410-km discontinuity is also shown.

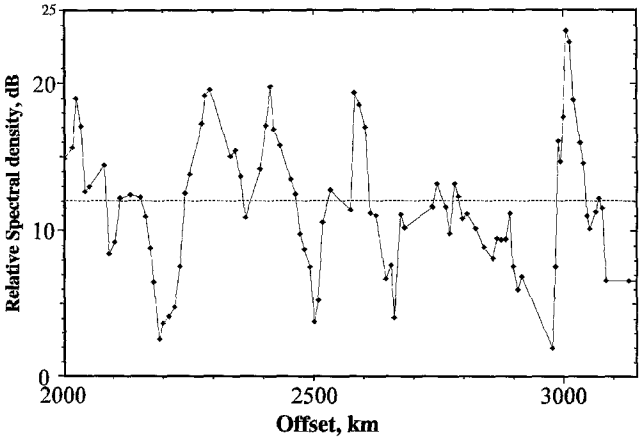

Figure 10. Spectral ratio of the teleseismic P_n to the first arrivals defined in equation (2), measured for 1- to 3-Hz and 4- to 6-Hz frequency intervals within the offset range between 2200 and 3000 km. Note that the high-frequency content of the teleseismic P_n phase exceeds the corresponding level in the first arrivals by about 4 to 20 dB, with an average of 12 dB (dashed line).

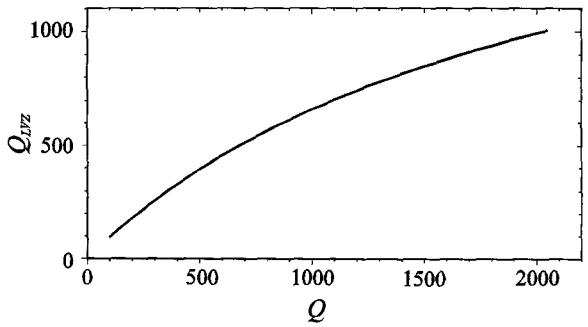

Figure 11. Constraint on the attenuation contrast at the top of the LVZ obtained from the ratios of power spectra of deep refractions and of the teleseismic P_n using equation (2). Q and Q_{LVZ} denote the quality factor above and below the depth of 150 km, respectively.

Although the presence of the attenuation contrast at the top of the LVZ is confidently established through the observed contrast in the frequency contents of the signals (Fig. 10), its simple estimate presented earlier can be improved in two ways: (1) The constraint shown in Figure 11 most likely *underestimates* the attenuation contrast, since we have assumed that the zone of high attenuation extends to the depth of 410-km discontinuity, whereas this zone can actually be thinner. (2) Not only the relation $Q_{LVZ}(Q)$ but also the values Q_{LVZ} and Q themselves can be measured from the records, yielding an independent way of obtaining a high-resolution image of the upper mantle attenuation structure. We will address these issues in a forthcoming article.

The physical causes of the observed mantle attenuation might be scattering by mantle heterogeneities as well as inelastic energy dissipation. However, the clear onset of the high-frequency energy (Fig. 4) suggests that the increase of attenuation below the level of 150 km occurs predominantly due to the increase in the intrinsic (inelastic) attenuation. Indeed, elastic scattering tends to delay the arrival of high-frequency energy, while intrinsic absorption removes it from the wave field (Richards and Menke, 1983). The records show that the increase of the high-frequency energy is strongly correlated with the WG modes and is not related to the scattering from the deeply refracted waves (Fig. 9). Even if the scattering mantle heterogeneities were located above the depth of 150 km, as Ryberg *et al.* (1995) have suggested, they would produce some pattern of high-frequency scattered energy following the first arrivals that is not found in the records.

Multiples and Scattering

The above travel-time simulations correctly indicate the position of the onset of the teleseismic P_n but do not account for the diffuse onset of this phase and for the presence of a long incoherent coda. These features can be explained by the scattering occurring within the crust and/or upper mantle.

To allow the propagation of high-frequency energy to substantial distances, the scattering within the uppermost mantle should be weak. An alternative proposed and modeled by Tittgemeyer *et al.* (1996) is a layered structure exhibiting strong multiple scattering in the vertical direction and almost no scattering horizontally. Although possible, this alternative does not seem to be likely, since it would imply a very high aspect ratio of the heterogeneities.

On the contrary, the crust represents a wave guide trapping postcritical P_g and S_g waves and propagating them to large distances. The Moho irregularities, surface and basement topography, and the variations in the crustal velocity along the profile (Schueller *et al.*, 1997) provide the heterogeneities that should be sufficient to generate the teleseismic P_n coda. Assuming that the scattering is moderate, we can use low-order Born approximations to estimate its influence on the pattern of the recorded wave field.

In our modeling, we analyze only the kinematics of the scattering by shooting pairs of rays from scattering points in random directions and by constructing a scattering pattern for each phase shown in Figure 5. The scatterers' depths and scattering angles are uniformly distributed, and thus the modeled offset–travel-time pairs build up a pattern of probable scattering paths from point scatterers. To produce a more physically realistic picture of scattering including scattering amplitudes, a more rigorous modeling using a 2D mantle velocity/attenuation model is certainly required.

The results of raytracing in the same 1D velocity model (Fig. 7) with random scattering heterogeneities located within the crust are shown in Figure 12. In our simulation, we included the first multiples from the free surface and from the Moho boundary (Fig. 5). Figure 12 shows that even first-order scattering within the crust complemented by multiples might account for the about 20-sec-long codas of the WG modes. This scattering also creates long trains of P_g energy lasting for about 40 to 50 sec in our simulation (note, however, that from the amplitude considerations, the dominant contribution to the coda should come from P-to-S_g scattering). Since up to 3 to 4 crustal multiples are observed in PNE records (Fig. 2), we expect that the real scattering pattern involving 3 to 4 scattering and free-surface/Moho/basement reflection events would be much more complicated and extended in time.

Coda

The high-pass filtered records show a long coda following the teleseismic P_n arrival (Fig. 4) apparently different from the amplitude pattern in the unfiltered records (Fig. 2). However, as Figure 13 shows, this difference is not so significant. In Figure 13, we present averaged amplitude decay curves measured within the offset range of 2500 to 2600 km, using the standard rms measure of the vertical component and a three-component instantaneous vector measure (Morozov and Smithson, 1996). In both cases, the signal was

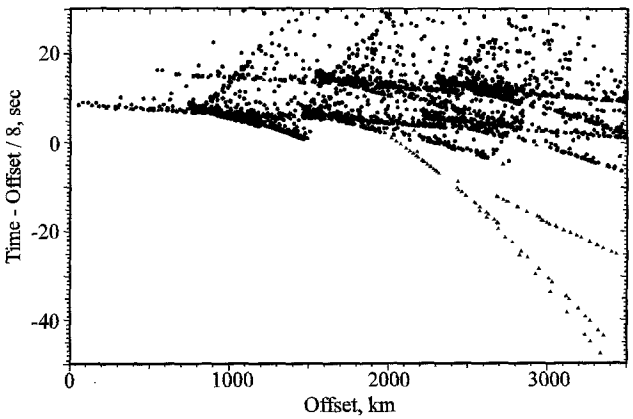

Figure 12. Travel-time plots obtained using raytracing in the 1D velocity model shown in Figure 7 with first-order random scatterers located within the crust. Note that already a single scattering within the crust is kinematically sufficient to account for observed codas of WG modes.

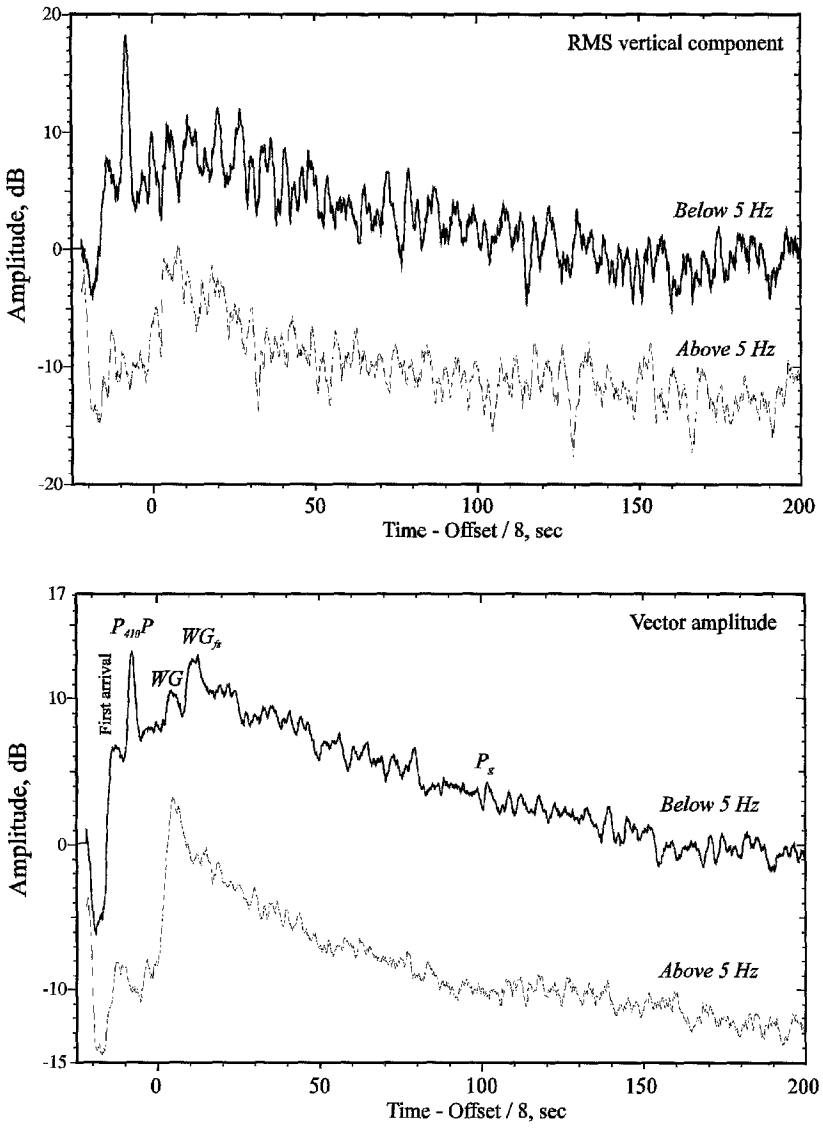

Figure 13. Amplitude decay curves of the high-frequency and low-frequency (filter corner frequency in both cases is 5 Hz) coda averaged within the offset range 2500 to 2600 km from PNE 323. (*Top*) rms amplitude of the vertical component; (*bottom*) three-component vector amplitude (Morozov and Smithson, 1996). In both cases, 8-km/sec time reduction was applied, and the traces were stacked; after that, trace amplitude was calculated and averaged within a 2-sec sliding time window. Note that the vector measure provides considerably more stable amplitude measurements. First arrivals and two WG phases are indicated. Note that the high-frequency coda of WG mode is somewhat *shorter* than the coda at low frequencies.

filtered below or above 5 Hz, and the amplitude was averaged within a 2-sec sliding time window. Similar to what has been observed by Kennett (1993), the vector measure provides significantly more stable amplitude estimates.

The amplitude decay plots in Figure 13 show that the teleseismic P_n is represented by a peak similar in duration to the onset of the first arrivals, followed by a long (up to 200 sec) train of crustal reverberations. Note that the high-frequency component actually decays a little *faster* than the low-frequency component, which is consistent with higher attenuation and scattering losses for shorter wavelengths. For both low-frequency and high-frequency components of the coda, the amplitude decay rate is close to $time^{-1/2}$ (Fig. 13), corresponding to the propagation of surface or guided waves. As outlined in the previous section, by far the most likely wave guide for these waves is represented by the crust. P_n and WG waves approaching the crust at grazing angles of incidence are strongly coupled to the relief on the Moho, on the top of the basement, on the free surface, as well as to crustal heterogeneities, generating postcritical shear-wave energy that is favored for lateral propagation in the crust (Dainty and Schultz, 1995). Also, an examination of the low-frequency records in Figure 2 shows that the coda of the WG mode is structured, including a sequence of prominent Moho multiples and higher-order WG modes.

Discussion

Our interpretation of the teleseismic P_n phase observed in the records from Quartz PNEs differs significantly from the interpretation of the same phase by Ryberg *et al.* (1995) and leads to a dramatically different (although more conventional) upper mantle model. Therefore, a discussion of the differences of these models is necessary. We focus this discussion on several principal aspects of the interpretation.

Physics of Wave Propagation. The "scattering wave guide" proposed by Ryberg *et al.* (1995) still needs to prove

its viability through a theoretical analysis or 2D/3D finite-difference simulation. From a general wave-propagation standpoint, scattering does not seem to be able to provide a sufficient mechanism to ensure a predominantly horizontal propagation of seismic energy. One-dimension simulations by Tittgemeyer *et al.* (1996) used as an evidence for a "totally new" phase describe a *totally different* physical situation of a stack of infinite thin layers that of course *do* form a wave guide. On the contrary, the well-established velocity gradient and the presence of the strong Moho and free-surface reflectors ensure an efficient propagation of the low-order WG modes.

Travel-Time Characteristics. Our interpretation accounts for three observed features of the teleseismic P_n travel-time character: (1) the increased moveout between the offsets of 1000 and 1500 km, (2) the presence of two branches corresponding to different orders of WG modes, and (3) the presence of high-frequency energy 7 to 10 sec before the main branch at the offsets exceeding 2700 km (Fig. 4). These details were not considered by Ryberg *et al.* (1995) and were not explained by the scattering wave-guide theory.

Amplitude Characteristics. Although a rigorous amplitude analysis of DSS data still presents a formidable problem, it can be seen that the observed amplitude pattern of the teleseismic P_n does not correspond to the model of a shallow scattering wave guide. Indeed, since the wave guide propagates the energy horizontally from the near-shot region, the amplitude of the phase would be expected to decrease continuously with distance. In the records of Figure 4, however, we see that the teleseismic P_n appears essentially after the onset of the $P_{90M}P$, which corresponds well to its interpretation as the WG mode.

The Sharpness of the Teleseismic P_n Onsets. The main point of the argument by Ryberg *et al.* (1995) against the WG interpretation is the absence of sharp onsets of the teleseismic P_n in the high-pass filtered records. However, an examination of both unfiltered (Fig. 2) and high-pass filtered records (Fig. 4) shows that the teleseismic P_n is sharp where it approaches the first arrivals (between the offsets of 1000 and 1600 km). In the records from PNE 123, a coherent first WG phase is seen even before its triplication point (Fig. 3). The teleseismic P_n becomes incoherent in the secondary arrivals, after its enhancement by heavy filtering (Fig. 4). Such behavior can be explained as due to various reasons:

1. The PNE source signature is far from a minimum-delay signal, and therefore, the signal remaining after the removal of most of its (low-frequency) energy may have no sharp onset.
2. Scattering within the crust makes the onsets of high-frequency phases complicated by long codas and diffuse (Fig. 12).
3. The high-frequency teleseismic P_n interferes with the background of energy following the strong first arrivals, which also contributes to the variability of its onset.
4. The top of the basement, not considered in our simulations, also presents a strong reflector creating numerous multiples and *P/S* conversions that cannot be resolved at the scale of this experiment.
5. With trace spacings exceeding 10 km, the data are strongly spatially aliased at 5 Hz, and therefore, we cannot expect to observe significant spatial coherency.

Due to these reasons, we find that the fine-scale shapes of the onsets of the teleseismic P_n do not carry any evidence against our WG model, and also, they do not require multiple scattering within the mantle for their explanation.

Coda. An over 20-sec-long coda of the teleseismic P_n arrival forms the second basis of the argument by Ryberg *et al.* (1995) and Tittgemeyer *et al.* (1996) against its WG origin. However, their analysis showing that the coda cannot be built up of WG branches was based on 1D simulations using the *reflectivity* technique. On the contrary, our measurement of the coda amplitude decay rate carried out above suggests that the coda can be satisfactorily explained by crustal-guided waves (L_g, R_g) propagating within the crust, in a manner similar to the explanations of regional *P*-wave codas (see, e.g., Dainty and Schultz, 1995).

Synthetic seismograms calculated using the *reflectivity* method (see Fig. 7 in Mechie *et al.,* 1993) show strong first WG and clear first free-surface WG modes supporting our raytracing analysis. Due to the limitations of the algorithm (truncation errors, numerical underflow, and computation time), a robust computation of the amplitudes of the higher-order WG modes arriving between the offsets of 2000 and 3000 km still presents a difficulty. Also, these amplitudes should be sensitive to the horizontally heterogeneous structure of the upper mantle not accounted for in 1D models employed by the *reflectivity* approach. Nevertheless, our conclusion about the increased attenuation within the LVZ will remain valid regardless of the amplitude modeling technique, since it is based on the basic observation obtained directly from the data—the seismic phases that arrive earlier are attenuated stronger.

Conclusions

Based on our analysis of the secondary phases observed in the records from the PNEs of the ultralong DSS profile Quartz, we propose an interpretation of a long-range (teleseismic) P_n phase as a whispering-gallery wave traveling within the uppermost mantle. This conclusion is supported by the 2D travel-time forward modeling of all observed phases using a detailed 1D velocity model derived earlier. The long incoherent coda of this phase is associated with the scattering and reverberations of seismic waves within the

crust, including its basement and the sedimentary cover. To explain the difference in the frequency contents between the teleseismic P_n and other refracted and reflected phases recorded at offsets exceeding 2000 km, we infer an increase in attenuation within the prominent low-velocity structures beginning at the depth of about 150 km. No scattering within the uppermost mantle is required to explain the observed characteristics of the wave field, and absorption is the most likely mechanism of the attenuation increase.

Acknowledgments

The acquisition of Quartz data was carried out by the Center GEON, Moscow, Russia (The Special Geophysical Expedition at the time of data acquisition). We thank E. Kazachenko, O. Ganzha, and other staff members of GEON, who digitized the data and provided other necessary information. A. Egorkin and N. Pavlenkova shared with us their experience in the interpretation of Quartz and other DSS data. The manuscript was greatly improved by the comments of Roger Bowman.

Our work on this project was sponsored by the Air Force Office for Scientific Research under Grants F49620-94-1-0134 and F49620-94-A-0134.

References

Anderson, D. L. and J. W. Given (1982). Absorption band Q model of the Earth, *J. Geophys. Res.* **87,** 3893–3904.

Cerveny, V., L. Klimes, and I. Psencik (1984). Paraxial ray approximation in the computation of seismic wavefields in inhomogeneous media, *Geophys. J.* **79,** 80–104.

Dainty, A. M. and C. A. Schultz (1995). Crustal reflections and the nature of regional P coda, *Bull. Seism. Soc. Am.* **85,** 851–858.

Egorkin, A. V. and A. V. Mikhaltsev (1990). The results of seismic investigations along geotraverses, in *Super-Deep Continental Drilling and Deep Geophysical Sounding,* K. Fuchs, Y. A. Kozlovsky, A. I. Krivtsov, and M. D. Zoback (Editors), Springer, Berlin, 111–119.

Egorkin, A. V. and N. I. Pavlenkova (1981). Studies of mantle structure in the U.S.S.R. territory on long-range seismic profiles, *Phys. Earth Planet. Interiors* **25,** 12–26.

Fuchs, K. and G. Müller (1971). Computation of synthetic seismograms with the reflectivity method and comparison with observations, *J. R. Astr. Soc.* **23,** 417–433.

Heustis, S., P. Molnar, and J. Oliver (1973). Regional S_n velocities and shear velocity in the upper mantle, *Bull. Seism. Soc. Am.* **63,** 469–475.

Kennett, B. L. N. (1993). The distance dependence of regional phase discriminants, *Bull. Seism. Soc. Am.* **83,** 1155–1166.

Kozlovsky, Y. A. (1990). The USSR Integrated Program of Continental Crust Investigations and Studies of the Earth's Deep Structure under the Globus Project, in *Super-Deep Continental Drilling and Deep Geophysical Sounding,* K. Fuchs, Y. A. Kozlovsky, A. I. Krivtsov, and M. D. Zoback (Editors), Springer, Berlin, 90–103.

Mantovani, E., F. Schwab, H. Liao, and L. Knopoff (1977). Teleseismic S_n: a guided wave in the mantle, *Geophys. J. R. Astr. Soc.* **51,** 709–726.

Mechie, J., A. V. Egorkin, K. Fuchs, T. Ryberg, L. Solodilov, and F. Wenzel (1993). P-wave velocity structure beneath northern Eurasia from long-range recordings along the profile Quartz, *Phys. Earth Planet. Interiors* **79,** 269–286.

Menke, W. H. and P. G. Richards (1980). Crust-mantle whispering gallery phases: a deterministic model of teleseismic P_n wave propagation, *J. Geophys. Res.* **85,** 5416–5422.

Molnar, P. and J. Oliver (1969). Lateral variations of attenuation in the upper mantle and discontinuities in the lithosphere, *J. Geophys. Res.* **74,** 2648–2682.

Morozov, I. B. and S. B. Smithson (1996). Instantaneous polarization attributes and directional filtering, *Geophysics* **61,** 872–881.

Morozova, E. A., I. B. Morozov, and S. B. Smithson (1997). Heterogeneity of the uppermost Eurasian mantle along the DSS profile 'Quartz', Russia, in *Upper Mantle Heterogeneities from Active and Passive Seismology,* K. Fuchs (Ed.), ISSBN 0-7923-4877-X, Kluwer Academic Publishers, Dordrecht, 139–146.

Richards, P. G. and W. Menke (1983). The apparent attenuation of a scattering medium, *Bull. Seism. Soc. Am.* **73,** 1005–1022.

Ryaboy, V. (1989). Upper mantle structure studies by explosion seismology in the USSR, Delphic Associates, 138 pp.

Ryberg, T., K. Fuchs, A. V. Egorkin, and L. Solodilov (1995). Observations of high-frequency teleseismic P_n on the long-range Quartz profile across northern Eurasia, *J. Geophys. Res.* **100,** 18151–18163.

Ryberg, T., F. Wenzel, J. Mechie, A. Egorkin, K. Fuchs, and L. Solodilov (1996). Two-dimensional velocity structure beneath Northern Eurasia derived from the super long-range seismic profile Quartz, *Bull. Seism. Soc. Am.* **86,** 857–867.

Schueller, W., I. B. Morozov, and S. B. Smithson (1997). Crustal and uppermost mantle velocity structure of northern Eurasia along the profile Quartz, *Bull. Seism. Soc. Am.* **87,** 414–426.

Sereno, T. J. and J. A. Orcutt (1985). Synthesis of realistic oceanic P_n wave trains, *J. Geophys. Res.* **90,** 12755–12776.

Sereno, T. J. and J. A. Orcutt (1987). Synthetic P_n and S_n phases and the frequency dependence of Q of oceanic lithosphere, *J. Geophys. Res.* **92,** 3541–3566.

Stephens, C. and B. L. Isacks (1977). Toward an understanding of S_n: normal modes of Love waves in an oceanic structure, *Bull. Seism. Soc. Am.* **67,** 69–78.

Sutton, G. H. and D. A. Walker (1972). Oceanic mantle phases recorded on seismograms in the northwestern Pacific at distances between 7° and 40°, *Bull. Seism. Soc. Am.* **62,** 631–655.

Tittgemeyer, M., F. Wenzel, K. Fuchs, and T. Ryberg (1996). Wave propagation in a multiple-scattering upper mantle—observations and modeling, *Geophys. J. Int.* **127,** 492–502.

Walker, D. A. (1977). High-frequency P_n and S_n phases recorded in the western Pacific, *J. Geophys. Res.* **82,** 3350–3360.

Department of Geology and Geophysics
University of Wyoming
P.O. Box 3006
Laramie, Wyoming 82071-3006
(I.B.M., E.A.M., S.B.S.)

Centre for Regional Geophysical and Geoecological Research (GEON)
Moscow, Russia
(L.N.S.)

Manuscript received 30 April 1997.